

## Thermoelectric Properties of $\text{YbZn}_{11-x}\text{Al}_x$

Shuai Li<sup>a</sup>, Ruhul Quddus<sup>b</sup>, Sree Sourav Das<sup>b</sup>, Haobo Wang<sup>a</sup>, Jerrold A. Floro<sup>a</sup>, and Mona Zebarjadi<sup>a,b</sup>

Received 00th January 20xx,  
Accepted 00th January 20xx

DOI: 10.1039/x0xx00000x

Metallic thermoelectric materials with high thermoelectric power factor and high thermal conductivity are favorable for transient dynamic active thermal management of microelectronics. Among these, several ytterbium intermetallic compounds demonstrate sharp peaks in their density of states due to contributions from ytterbium f-orbitals.  $\text{YbZn}_{11}$  is one of these compounds with a Gaussian-like density of states close to its Fermi level, an advantageous shape to achieve a large thermoelectric power factor. If the Fermi-level can be adjusted, large Seebeck coefficient values are expected following the Wiedemann-Franz law. Here we present  $\text{YbZn}_{11}$ , a rarely made and studied sample, and for the first time, we report its thermoelectric and transport properties. Band structure calculations confirm the Gaussian function shape of the density of states. However, Seebeck calculations show that the Fermi level is not well positioned and ideally should be shifted by 200 meV. Al substitution for Zn ( $\text{YbZn}_{11-x}\text{Al}_x$ ) and Zn- deficiency ( $\text{YbZn}_{11-x}$ ) are applied to modify the band structure and to shift the Fermi level to adjust the Seebeck coefficient.

### 1. Introduction

State-of-the-art electronics featuring high-power chips pack gigahertz transistors in an extremely dense manner. The substantial heat accumulated in such a small area presents new challenges for thermal management.<sup>1–3</sup> The concept of the thermoelectric (TE) active cooling mode provides innovative approaches for active heat management.<sup>4,5</sup> Unlike traditional thermoelectric modes with the Seebeck voltage (Peltier current) working against the temperature gradient, in active cooling mode, the natural heat conduction from the hot source to the heat sink is enhanced by the Peltier current. The Peltier current, enforced by the electric current, propels carriers along the temperature gradient, augmenting the passive transport of electrons and phonons. The TE module functions as an active heat sink. The effective thermal conductivity of this active heat sink under optimal current conditions is expressed as  $\kappa_{eff} = \left( \kappa + \frac{\sigma S^2 T_H^2}{2\Delta T} \right)$ , where  $T_H$  is the hot source temperature,  $\Delta T$  is the temperature difference between the hot source and the heat sink,  $\kappa$  is the passive thermal conductivity,  $\sigma$  is the electrical conductivity, and  $S$  is the Seebeck coefficient.<sup>5</sup> Hence to maximize the effective thermal conductivity, materials with large TE power factors ( $\sigma S^2$ ) and large passive thermal conductivity values ( $\kappa$ ) are needed.

Metals are great candidates for this application due to their inherently large electrical and thermal conductivity. Their only drawback is their low Seebeck coefficient. Hence, one can search for metals with large Seebeck coefficients to satisfy all

criteria needed for successful active cooling. Pure metallic elements such as cobalt and nickel are shown to have a relatively large Seebeck coefficient. Various mechanisms can improve the Seebeck coefficient in metals. For instance, in the case of cobalt, the large Seebeck coefficient is attributed to the magnon-drag effect.<sup>4</sup> In  $\text{CePd}_3$  the electron correlation effect results in a Seebeck coefficient of more than  $115 \mu\text{V}/\text{K}$  at 150K.<sup>4</sup> The Kondo resonance caused by the interaction of Yb 4f-orbital electrons and conduction bands gives  $\text{YbAl}_3$  a Seebeck of  $-90 \mu\text{V}/\text{K}$  below room temperature.<sup>6</sup> Cu-Ni alloy, also known as Constantan, shows improved Seebeck of  $-45.7 \mu\text{V}/\text{K}$  at room temperature and  $-72.5 \mu\text{V}/\text{K}$  at 873K due to the scattering of low-energy carriers by nano-twin boundaries.<sup>7</sup> Further study explored the possibility of additive manufacturing of Cu-Ni alloy using industrial-level powders.<sup>8</sup> An even higher Seebeck of  $94 \mu\text{V}/\text{K}$  is achieved in Ni-Au alloy at 1000K, which is attributed to the interband scattering between s and d-orbital electrons.<sup>9</sup> In metals, the Mott Formula<sup>10</sup> relates the Seebeck coefficient to the slope of the density of states (DOS) at the Fermi level. For metals, therefore, a sharp peak of the DOS near the Fermi level indicates the potential of a high Seebeck coefficient.<sup>11–14</sup> Some of the Yb-based intermetallic compounds show such features according to **first-principles** calculations. A good example is  $\text{YbAl}_3$  which has a sharply peaked DOS due to the f-orbitals and as a result, has a record high thermoelectric power factor.<sup>15</sup>  $\text{YbZn}_{11}$  is another candidate in this class of materials. Since its crystal structure was first reported in 1966<sup>16</sup>,  $\text{YbZn}_{11}$  has received little attention. Apart from a few studies that mention it while exploring the phase space of related systems<sup>17,18</sup>, the only paper discussing its inter-band interaction dates to 1998<sup>19</sup>. Moreover, the thermoelectric properties of  $\text{YbZn}_{11}$  have never been thoroughly examined or reported.

The expected sharp peaks in the DOS of several intermetallic Yb-based compounds are confirmed within the Topological Materials Database<sup>20–22</sup> band structure calculations.<sup>13,15,16</sup> Similarly, in  $\text{YbZn}_{11}$ , a sharp peak of DOS near the Fermi level is

<sup>a</sup> Department of Materials Science and Engineering, University of Virginia, Charlottesville, VA, 22904, United States

<sup>b</sup> Electrical and Computer Engineering Department, University of Virginia, Charlottesville, VA, 22904, United States

† Footnotes relating to the title and/or authors should appear here.

Electronic Supplementary Information (ESI) available: [details of any supplementary information available should be included here]. See DOI: 10.1039/x0xx00000x

shown in the topological materials database which in principle should result in a large Seebeck coefficient as evidenced by the Mott equation. However, this material is rarely studied, and its thermoelectric properties have never been reported. To assess the guidance provided by computational results and investigate the unreported thermoelectric properties of the materials, we synthesized YbZn<sub>11</sub>. Here, we report structural characterization and assessment of defects, followed by intrinsic thermoelectric properties. Finally, we explore avenues to enhance the thermoelectric performance using doping.

## 2. Methods

### 2.1 Experimental Methods

Sublimed Yb pieces with 99.9% purity and 99.999% zinc shot were mixed to the stoichiometry of YbZn<sub>11</sub>. The mixed pure metals were loaded into a fused quartz glass tube. The tube was evacuated and backfilled with Argon three times, then sealed. The sealed ampoule was heated up to 890°C to melt the metal for 16 hours, then kept at 760°C for 16 hours. After cooling down the ingot is ground into powder with mortar and pestle. Ball-milling was not attempted due to the reactive nature of ytterbium. X-ray Diffraction (XRD) was performed on powders and hot-pressed samples to confirm the formation of the compound. Al was used to substituting Zn to adjust the Fermi level. 99.999% aluminium powder and wires were added according to stoichiometry. The intrinsic and YbZn<sub>10.7</sub>Al<sub>0.3</sub> samples were annealed at 650°C in a sealed tube for 24 hours, to improve the Al distribution and substitution. For each sample around 2.5 grams of the product powder was loaded in a graphite die, with graphite paper covering the inner wall and the interface between the powder and the pushing rod to prevent sticking. The powders were then hot-pressed at 650°C under 56 MPa pressure for 300 seconds using an OTF-1700X-RHP4 hot-press setup from MTI Corporation. The hot press chamber was filled with argon gas during the process. A disc-shaped solid sample with a diameter of 12.7 mm was obtained after polishing the hot-pressed ingot. The disc-shaped sample was then cut by a Mager BR220 precision cut-off saw into bar-shaped samples with approximate 2mm × 2mm × 10mm dimensions. Transport performance is performed using the Quantum Design PPMS Versalab. The XRD characterization is performed using an Empyrean X-ray diffractometer from Malvern-Panalytical on a pressed disc sample. Imaging is performed on an FEI Quanta 650 Scanning Electron Microscope (SEM).

### 2.2 Computational Methods

YbZn<sub>11</sub> crystallizes in a tetragonal I4<sub>1</sub>/amd space group with 2 Yb and 22 Zn atoms in the unit cell. The lattice parameters were nominally a=b=10.66 Å and c=6.383 Å from the topological materials database<sup>1</sup>. **First-principles** calculations were performed using the density functional theory (DFT) as implemented in the QUANTUM ESPRESSO package.<sup>23</sup> We used Perdew-Burke-Ernzerhof generalized gradient approximation (PBEsol)<sup>24</sup> pseudopotential for Zinc (Zn) and Wentzcovitch (PAW) pseudopotential<sup>25</sup> for Ytterbium (Yb). Scalar relativistic

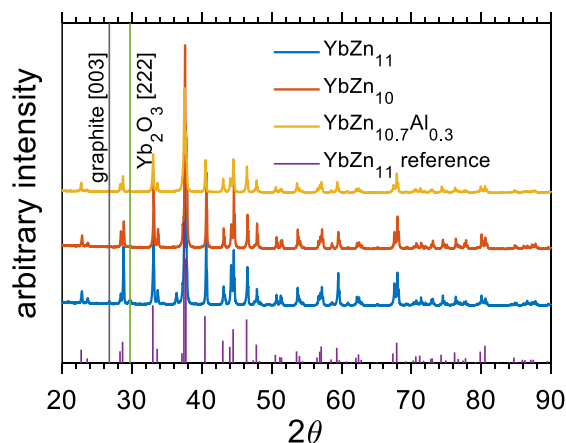


Figure 1. XRD results of Yb-Zn samples, annealed intrinsic YbZn<sub>11</sub> sample in blue, Zn-deficient sample YbZn<sub>10</sub> sample in orange, and Al-substitution sample YbZn<sub>10.7</sub>Al<sub>0.3</sub> in yellow, and the reference peaks in purple<sup>29</sup>. Minor impurity peaks from graphite and ytterbium oxide are marked by black and green lines.

pseudopotentials were used throughout the calculation as we found no spin-orbit coupling (SOC) effects on electronic band structure as shown in supplementary information Figure S2. The electronic structure calculation employed a kinetic energy cutoff of 60 Ry with a charge density cutoff of 320 Ry and a Monkhorst-Pack k-point mesh of 8×6×6. The atomic positions were relaxed through the Broyden–Fletcher–Goldfarb–Shanno (BFGS algorithms). The convergence threshold of energy was set to 4.8×10<sup>-9</sup> Ry in the self-consistent calculation. A Gaussian smearing value of 0.01 Ry was chosen during the calculations. Finally, the Seebeck coefficient was evaluated using the BoltzTraP package.<sup>26</sup> BoltzTraP solves the Boltzmann Transport Equations (BTE) under constant relaxation time approximation.<sup>26</sup> Within the constant relaxation-time approximation, the Seebeck coefficient can be obtained directly from the electronic structure without any adjustable parameters, and it is expressed in the following equation:

$$S_{\alpha\beta}(T, \mu) = \frac{1}{eT\Omega\alpha_{\alpha\beta}(T, \mu)} \int \sigma_{\alpha\beta}(\varepsilon)(\varepsilon - \mu) \left[ -\frac{\delta f_0(T, \varepsilon, \mu)}{\delta \varepsilon} \right] d\varepsilon \quad (1)$$

where  $\Omega$  is the cell volume,  $e$  is the electron charge,  $\mu$  is the chemical potential,  $\varepsilon$  is the electron energy, and  $T$  is the absolute temperature.  $f_0$  is the equilibrium Fermi-Dirac distribution function and  $\sigma_{\alpha\beta}$  is the transport distribution tensor with  $\alpha$  and  $\beta$  as the tensor indices indicating the crystallographic directions.  $\sigma_{\alpha\beta}(\varepsilon)$  is also referred to as the differential conductivity and is  $\sigma_{\alpha\beta}(\varepsilon) = v_g^2 \tau(\varepsilon) g(\varepsilon)$ , where  $v_g$  is the group velocity,  $\tau$  is the scattering time, and  $g(\varepsilon)$  is the DOS. Under constant relaxation time approximation used here,  $\tau(\varepsilon) = \tau_0$  and is a constant and the elements of conductivity tensor are calculated using the Fourier interpolation of the band structure only.

## 3. Results and discussion

### 3.1 Material Characterization

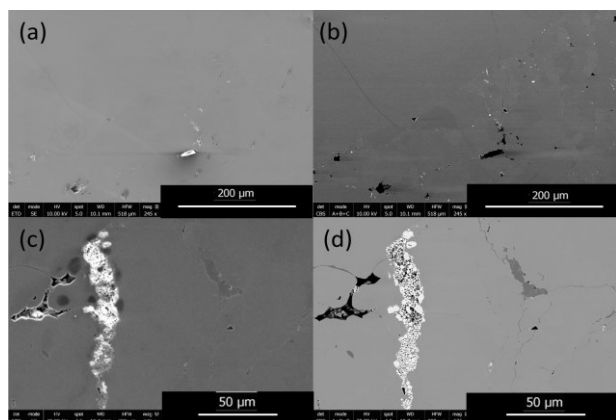


**Figure 2.** (a) and (b) are the secondary electron (SE) image and back-scattered electron (BSE) image of  $\text{YbZn}_{11}$  sample at a larger scale (with a scale bar of  $200\mu\text{m}$ ) at the same site. The bright feature shown in SE image (a) is charging from a glass fragment coming from the synthesis process, which can be confirmed by the fact that the BSE image shows a low electron count from back-scattering, indicating low mass elements. (c) and (d) are SE and BSE images at higher magnification (scalebar of  $50\mu\text{m}$ ) on typical defects.

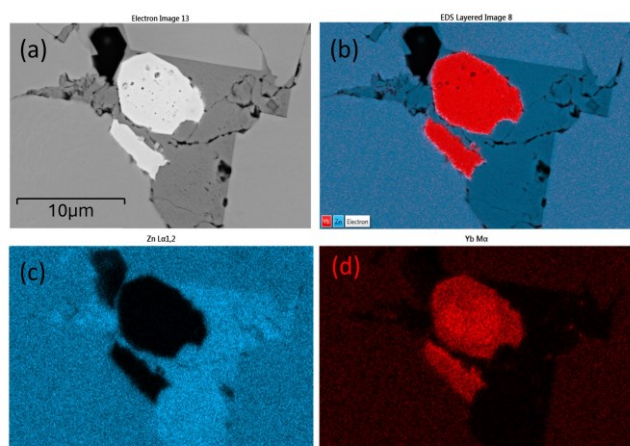


**Figure 3.** EDS mapping. (a) BSE image of a typical defect site with cavities (black), Yb oxides (white), Zn (dark grey), compared to  $\text{YbZn}_{11}$  (light grey). (b) layered EDS map, (c) Zn distribution EDS map, (d) Yb distribution map. The blue and red dots density in (c) and (d) represent the relative Zn and Yb concentration.

Many samples were prepared including intrinsic  $\text{YbZn}_{11}$ , Al-doped ones ( $\text{YbZn}_{11-x}\text{Al}_x$ ), and Zn-deficient ones ( $\text{YbZn}_{11-x}$ ).

The XRD results of three representative samples are shown in Figure 1. Note that in the patterns of  $\text{YbZn}_{11}$  and  $\text{YbZn}_{10.7}\text{Al}_{0.3}$ , two minor peaks of graphite and  $\text{Yb}_2\text{O}_3$  can be identified. The graphite peak comes from the residue of graphite paper during the hot press process and only exists at the surface. The residue can stay in small cavities during the polishing process. The oxide peaks may result from residual oxygen in the sealing process. All the relevant samples show excellent correspondence in XRD of the synthesized material with the standard diffraction pattern for  $\text{YbZn}_{11}$  and the impurities only appear in **small volume fraction** as indicated **by the few identifiable minor peaks** in XRD.

SEM micrographs from the  $\text{YbZn}_{11}$  sample in Figure 2 show the typical defects in these Yb-Zn intrinsic samples. Figures 2(a) and 2(b) show the secondary electron (SE) image and back-scattered

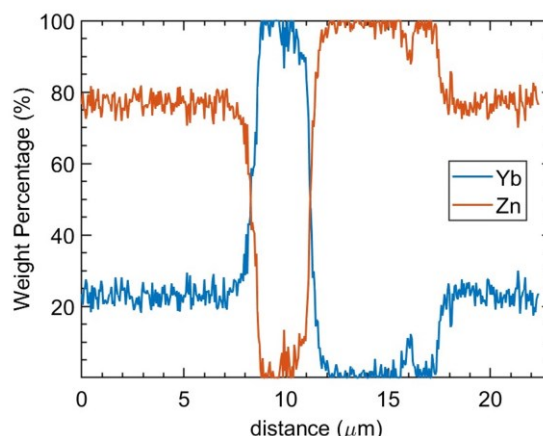
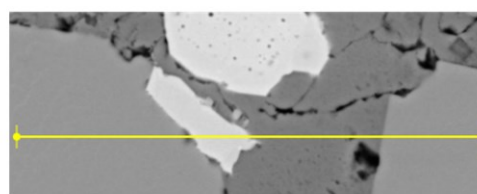


**Figure 4.** EDS line scan on the defect site. The scanning line goes through  $\text{YbZn}_{11}$  matrix, Yb oxides (white), Zn-rich phase (dark grey), and  $\text{YbZn}_{11}$ .

electron (BSE) image of the  $\text{YbZn}_{11}$  sample with a scalebar of  $200\mu\text{m}$ . Shown as the extended light grey area in the BSE image,  $\text{YbZn}_{11}$  constitutes the majority of material corresponding well with the XRD results. With higher magnification, (Figure 2(c) and 2(d), SE and BSE respectively) the impurities in the microstructure can be identified. Typical defects are pores (black), Yb-rich (white), and Zn-rich (dark grey).

The samples are sintered from hand-milled powders. The intrinsic limitation of this sintering process results in minor retained porosity, as shown in the BSE images. This observation is confirmed by the SE image, which illustrates the morphology. The mass density of the  $\text{YbZn}_{11}$  sample is measured to be 98% of the theoretical density indicating the presence of some pores. Small Yb pieces that remained un-melted during the melting process or precipitated after cooling down oxidized post-process, exhibiting higher brightness in the SE image due to the charging effect and in the BSE image owing to their higher relative mass.

In EDS mapping mode, the distribution of the elements can be demonstrated clearly as shown in Figure 3. All three types of defects: cavity(pores), Yb-rich, and Zn-rich phase are shown in one site. In Figure 3(b), Yb-rich, Zn-rich, and the pure  $\text{YbZn}_{11}$  phases are identified by the red, dark blue, and blue areas, respectively. Figures 3(c) and 3(d) show that the defects are caused by unreacted Yb and Zn. The dark grey area in Figure 3(a) shows a higher Zn concentration as confirmed in Figure 3(c) and near-zero Yb concentration as confirmed in Figure 3(d), indicating the existence of the Zn-rich phase. Similarly, the white area in Figure 3(a) seems to be majority Yb with almost no Zn. Here we postulate that these small defects are ytterbium oxide considering the reactivity of Yb,  $\text{Yb}_2\text{O}_3$  peaks in XRD, and the charging effect of this kind of defect under the electron beam. Further EDS line scan on the same site crossing all separate phases as shown in Figure 4 confirms the weight percentage of Yb and Zn in these phases. The main matrix shows

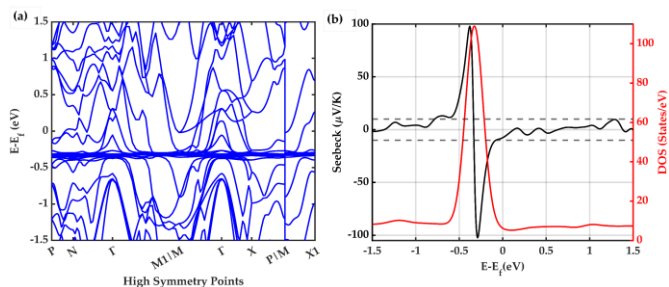


Figure 5. (a) Electronic Band Structure and (b) Seebeck and Density of States of  $\text{YbZn}_{11}$ .

the correct weight percentage of Yb and Zn for  $\text{YbZn}_{11}$ ,

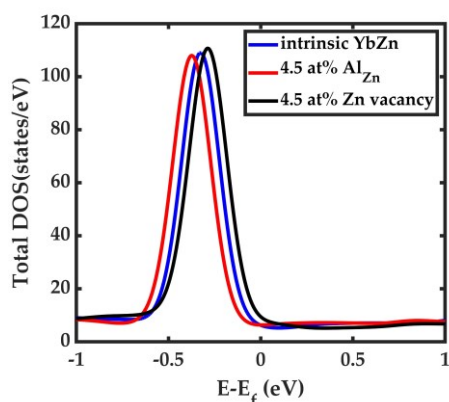


Figure 6. Effect of Al doping and Zn deficiency on the density of states. Al doping shifts the DOS to lower energy levels while Zn vacancy moves the DOS to higher energy levels.

combined with XRD results and EBSD results in Supplementary, the major matrix is confirmed to be  $\text{YbZn}_{11}$ .

Combining XRD and SEM results, the micron-sized oxide with extremely small volume fraction primarily appear in cavities. Considering the extended grain size of the  $\text{YbZn}_{11}$  crystals, (Figure S1), we believe the scattered oxide impurities should not significantly affect the overall transport properties nor the overall thermoelectric performance of macroscopic samples.

### 3.2 Band Structure Calculations

The electronic band structure and electronic density of states (DOS) calculated for intrinsic  $\text{YbZn}_{11}$  are shown in Figure 5. The band structure is shown in Figure 5(a) along high symmetry direction  $P(0.25,0.25,0.25)$ - $N(0,0.50,0)$ - $\Gamma(0,0,0)$ - $M1/M(-0.50,0.50,0.50)$ - $\Gamma(-X(0,0,0.50))$ - $P/M(0.50,0.50,0.50)$ - $X1(0,1.00,0.50)$ . The obtained DFT band structure and the DOS are in good agreement with previous calculations shown in the Topological Materials Database.<sup>27</sup> The density of states has a smeared delta-function (Gaussian) shape centred approximately 322 meV below the Fermi level. This is an ideal band structure shape for a thermoelectric material as was discussed by Mahan and Sofo.<sup>28</sup> However, the Fermi level ideally should be within a few  $k_B T$  from the peak point where the slope of the DOS with respect to energy is maximum.

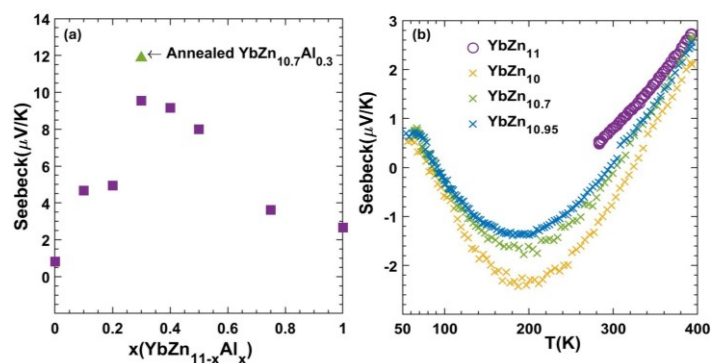


Figure 7. (a) Room temperature Seebeck of  $\text{YbZn}_{11-x}\text{Al}_x$  versus Al component  $x$ . The green triangle shows the annealed  $\text{YbZn}_{10.7}\text{Al}_{0.3}$ . (b) Seebeck of  $\text{YbZn}_{11-x}$  ( $x=0.05, 0.3, 1$ ) versus temperature from 70-400K

The Seebeck coefficient at room temperature (300 Kelvin) and the DOS are shown together in Figure 5(b). The Mott formula for the thermoelectric power  $S$  for metals is defined in the following equation:

$$S_{\alpha\beta} = \frac{\pi^2}{3} \left( \frac{k_B T}{e} \right) \left( \frac{d \ln \sigma_{\alpha\beta}(\epsilon)}{d\epsilon} \right)_{\epsilon = \mu} \quad (2)$$

Where  $k_B$  is the Boltzmann constant and the rest of the parameters are defined in Eq. 1. Under constant relaxation time approximation, Seebeck is directly proportional to the slope of the natural log of DOS. To achieve a high Seebeck coefficient, a large slope in the DOS near the chemical potential is required. Therefore, a delta function in a metallic material can potentially correspond to both large conductivity (due to large DOS) and large Seebeck coefficient (due to large slope of DOS) values. Here we note that the Seebeck coefficient has a range of -100 to 100  $\mu\text{V}/\text{K}$  in a narrow chemical potential range ( $\sim 500$  meV). The main problem in this sample is that the intrinsic Fermi level is not close enough to the peak of the DOS. As shown in Figure 5b, at the intrinsic level, the Seebeck coefficient is only -10  $\mu\text{V}/\text{K}$ . Hence, the experimental intrinsic Seebeck coefficient is expected to be small. To reach larger Seebeck values, therefore, careful adjustment of the Fermi level via alloying and doping is needed.

For example, Figure 6 demonstrates that upon doping with Al, we can shift the peak in the DOS to lower energies. Specifically, upon 4.5% Al doping, the peak is 371 meV below the Fermi level, which is 49 meV further away from the Fermi level compared to the intrinsic case. On the other hand, upon inclusion of zinc deficiency, we can move the peak toward the higher energies and closer to the Fermi level. Including 4.5% zinc vacancy shifts the peak to approximately -286 meV, bringing it closer to the Fermi level compared to the intrinsic case by 36 meV. In terms of the changes in the Seebeck coefficient, these two doping strategies should show opposite trends which we can confirm experimentally as will be discussed later. However, the predicted changes are not significant enough to increase the Seebeck coefficient significantly. To achieve a high Seebeck coefficient, the Fermi level must be shifted ideally to 202 meV below the intrinsic Fermi level where the slope of the DOS is the largest. There may be other promising transition metals that could serve as dopants to fine-tune the Fermi level. Further

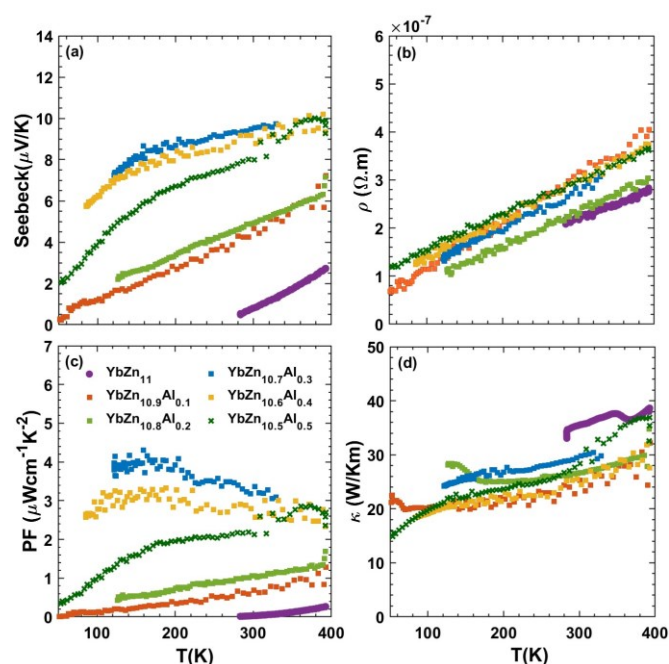


**Figure 8.** (a) Seebeck coefficient, (b) resistivity, (c) power factor, (d) thermal conductivity of  $\text{YbZn}_{11-x}\text{Al}_x$  samples ( $x=0, 0.1, 0.2, 0.3, 0.3, 0.4, 0.5$ ) versus temperature from 70K-400K.

research is necessary to optimally adjust the Fermi-level position, which will be the focus of future studies.

### 3.3 Performance

As discussed in the theoretical section, intrinsic  $\text{YbZn}_{11}$  is expected to have a low Seebeck coefficient. The room temperature value measured for intrinsic  $\text{YbZn}_{11}$  is only  $1 \mu\text{V}/\text{K}$ . Therefore, we attempted to tune the Fermi level via doping. We note due to the errors in theoretical calculations for small Seebeck values and the presence of defects in experimental samples, a direct quantitative comparison of theory and experiment is not possible, and we only can use theory to predict trends.

In Figure 7, the trend of measured room temperature Seebeck versus Al composition  $x$  ( $\text{YbZn}_{11-x}\text{Al}_x$ ) is demonstrated. The addition of a small amount of Al improves the Seebeck of  $\text{YbZn}_{11-x}\text{Al}_x$ , peaking at  $\text{YbZn}_{10.7}\text{Al}_{0.3}$ . A further increase in Al amount reduces the Seebeck coefficient. The low performance of samples with  $x$  larger than 0.3 could be attributed to the formation of other Yb-Al compounds due to limited solubility Al in  $\text{YbZn}_{11}$ . However, due to their low concentration, they are not identified in the XRD analysis. The Seebeck value peaks at  $x=0.3$ , reaching  $9.54 \mu\text{V}/\text{K}$  at 300K. After annealing, the Seebeck further increased by 24.4% to  $11.87 \mu\text{V}/\text{K}$ , which should be attributed to improved distribution and dissolution of Al in the Yb-Zn. Further high-temperature measurements after annealing are reported in the supplementary materials, Figure S3, indicating further small improvements in the Seebeck coefficient.

Figure 8 summarizes the trends of the transport properties, including the Seebeck coefficient, electrical resistivity, and thermal conductivity as a function of temperature from 50 to 400K for Al-doped samples. The uncertainty on the Seebeck coefficient is less than 15% and for resistivity, it is less than 10%.

These values are estimated by repeating the measurements under different thermal history conditions and are detailed in supplementary materials. As temperatures increase, the Seebeck coefficient and resistivity both increase, a common trend in all samples studied here and in general in the thermoelectric field. The increasing Seebeck coefficient can be explained by the Mott equation of metals (Eq. 2). Assuming no change in the slope of DOS with temperature, Seebeck should increase linearly with temperature. However, the relation is not exactly linear as the Fermi level position changes slightly with temperature. The increase in the resistivity can be explained by the increasing scattering between electrons and phonons at elevated temperatures. Finally, the thermal conductivity is dominated by the electronic contribution and follows Wiedemann-Franz law closely. At room temperature, the electronic contribution of the thermal conductivity is 93% for  $\text{YbZn}_{11}$  sample and 88% for  $\text{YbZn}_{10.7}\text{Al}_{0.3}$ . Details of lattice thermal conductivity calculations and relevant plots are presented in the supplementary materials.

The addition of the optimal amount of Al ( $x = 0.3-0.5$ ) altered the trend of the Seebeck coefficient versus temperature, particularly in the lower temperature range, resulting in a significant increase in the Seebeck coefficient. This increase is the primary reason for the enhanced power factor. The resistivities of all  $\text{YbZn}_{11-x}\text{Al}_x$  samples, closely resemble that of intrinsic  $\text{YbZn}_{11}$ , indicating only minor increases in scattering rates at low Al compositions. Further increasing the Al composition surpasses the solubility limit, and leads to different reactions during the melting process, resulting in the appearance of multiple crystalline oxides that increase the resistivity while the thermal conductivity remains close to intrinsic  $\text{YbZn}_{11}$ . More details are included in Supplementary materials (Figure S8, S9). The thermoelectric power factor of  $\text{YbZn}_{11-x}\text{Al}_x$  ( $x=0.3, 0.4$ ) peaks at around 100K to  $4 \mu\text{Wcm}^{-1}\text{K}^{-2}$  due to the decreased resistivity at low temperatures and the sharp increase of the Seebeck coefficient.

Other ways of altering the  $\text{YbZn}_{11}$  system such as non-stoichiometry composition  $\text{YbZn}_{10.9}$  and Ag and Sn substitution  $\text{YbZn}_{10.9}\text{Sn}_{0.1}$  have been tried. All show improvements but do not exceed the  $\text{YbZn}_{10.7}\text{Al}_{0.3}$  sample. Zn-deficient samples  $\text{YbZn}_{11-x}$  with  $x=0.05, 0.3, 1$  were prepared using the same methods as those of intrinsic and Al-substitution samples. As shown in Figure 7b, the introduction of Zn deficiency results in more negative Seebeck coefficient values. This is the opposite of what was observed with Al doping and is consistent with our theoretical results discussed in section 3.2. Since Al-doping results in a shift of the DOS delta function to lower energy values and Zn-deficiency does the reverse (see Figure 6), an opposite trend in the Seebeck coefficient is expected using these two doping strategies. While we can predict some trends using the first-principles approach, we acknowledge that a direct comparison between theory and experiment is not possible due to several factors. First, the as-grown  $\text{YbZn}_{11}$  in the experiment is different from the ideal intrinsic  $\text{YbZn}_{11}$  used in modelling, and the exact position of the Fermi level is unknown due to inherent low dimensional defects that are evenly distributed in the  $\text{YbZn}_{11}$  crystal grains such as vacancies, substitutional impurities, and interstitials. As shown in the supplementary materials, changes in the inherent atomic-level defects/impurities results in changes in the DOS which alters

the Seebeck coefficient at a given chemical potential. Second, the first-principles data generated has an error bar due to errors in band structure calculations and the constant relaxation time approximation used. As seen in Figure 8(a), the Seebeck coefficient does not show a linear trend with respect to temperature for many of the samples. This nonlinear trend can be attributed to temperature-dependent relaxation times as well as minor changes in the chemical potential with temperature and is discussed further in the supplementary materials. While we do not have a good way to estimate this error, the error in Seebeck calculations should be on the order of  $10 \mu\text{V}/\text{K}$  and therefore small Seebeck values as highlighted in the dashed-line region of Figure 5(b) have values close to the noise level of Seebeck calculations.

In the case of Zn deficiency, the value of the Seebeck coefficient is maximum at around 200K, but its value remains small. The vacancies lowered both thermal and electrical conductivity slightly and combined with its low Seebeck values, did not result in improvements larger than Al-doping. At  $x=1$  deficiency the hot-pressed sample shows a large level of cavities and poor sintering. Hence, Al-doping is identified as a better solution compared to the Zn-deficiency method. Similarly, Ag doping (not presented here) made the Seebeck coefficient more negative, however, Ag solubility is not good enough to significantly affect the Seebeck values toward large negative values.

## Conclusions

YbZn<sub>11</sub>-based samples were synthesized and confirmed using XRD and SEM methods. Small pores, Yb<sub>2</sub>O<sub>3</sub>, and zinc-rich defects were identified in the samples. The thermoelectric properties are reported for the first time. All samples have low resistivity confirming the metallic nature of the samples. The thermal conductivity of the samples is dominated by the electronic contribution as expected from metals with the intrinsic sample having a thermal conductivity of  $35 \text{ W m}^{-1} \text{ K}^{-1}$  at room temperature and further increasing with temperature. The downside of these samples is their low Seebeck coefficient values. Efforts to improve the Seebeck coefficient by Al substitution are conducted and resulted in improved Seebeck by an order of magnitude without sacrificing the electrical or thermal conductivity. However, the thermoelectric power factor remains modest with a peak value of  $4 \mu\text{W cm}^{-1} \text{ K}^{-2}$  at 100 K. First-principles calculations identified a Gaussian-shape DOS ideal for thermoelectric power factor in YbZn<sub>11</sub>. However, the Fermi level is not ideally positioned with respect to this Gaussian function and needs to be adjusted for high performance. The limited solubility of Al, Sn, and Ag prevented further adjustments to the Fermi level. Similarly, zinc-deficiency tuning of the Fermi level is limited and does not allow for adjusting the Fermi level far enough to verify the existence of the DOS peak and, therefore, the high performance. Further studies of other dopants and alloying are needed to adjust the Fermi level to increase the Seebeck coefficient.

## Author Contributions

SL: conceptualization, data curation, formal analysis, investigation, methodology, visualization, writing – original manuscript. RQ and SSD: simulation, validation, writing – original manuscript. HW: data curation, formal analysis. JF: methodology, supervision, writing-review&editing, MZ: conceptualization, funding acquisition, project administration, supervision, and writing – review & editing.

## Conflicts of interest

There are no conflicts to declare.

## Acknowledgments

RQ and SSD would like to acknowledge the Rivanna cluster of UVA used for the computational part. We acknowledge Xin Shi and Zhifeng Ren of the University of Houston for their help in verifying our results and for the high-temperature measurements presented in the supplementary materials. We acknowledge the Nanoscale Materials Characterization Facility (NMCf) at UVA for providing SEM and XRD facilities. This work is supported by NSF grant number 2230352.

## Data availability

Data for this article, including raw experimental measurements are available at YbZn<sub>11</sub> thermoelectric transport properties at <https://doi.org/10.18130/V3/QOPZXU>.

## Notes and references

- 1 Z. Zhang, X. Wang and Y. Yan, *e-Prime - Advances in Electrical Engineering, Electronics and Energy*, 2021, **1**, 100009.
- 2 S. M. Sohel Murshed and C. A. Nieto de Castro, *Renewable and Sustainable Energy Reviews*, 2017, **78**, 821–833.
- 3 H.-M. Tong, Y.-S. Lai and C. P. Wong Editors, .
- 4 M. J. Adams, M. Verosky, M. Zebarjadi and J. P. Heremans, *Phys Rev Appl*, 2019, **11**, 054008.
- 5 M. Zebarjadi, *Appl Phys Lett*, 2015, **106**, 203506.
- 6 H. J. van Daal, P. B. van Aken and K. H. J. Buschow, *Phys Lett A*, 1974, **49**, 246–248.
- 7 J. Mao, Y. Wang, H. S. Kim, Z. Liu, U. Saparamadu, F. Tian, K. Dahal, J. Sun, S. Chen, W. Liu and Z. Ren, *Nano Energy*, 2015, **17**, 279.

- 8 S. Li, K. Snyder, M. S. Akhanda, R. Martukanitz, M. Mitra, J. Poon and M. Zebarjadi, *Int J Heat Mass Transf*, 2022, **195**, 123181.
- 9 F. Garmroudi, M. Parzer, A. Riss, C. Bourgès, S. Khmelevskiy, T. Mori, E. Bauer and A. Pustogow, *Sci Adv*, , DOI:10.1126/SCIADV.ADJ1611/SUPPL\_FILE/SCIADV.ADJ1611\_SM.PDF.
- 10 N. F. Mott, E. A. Davis and K. Weiser, *Phys Today*, 1972, **25**, 55–55.
- 11 G. D. Mahan and J. O. Sofo, *Proceedings of the National Academy of Sciences*, 1996, **93**, 7436–7439.
- 12 J. Zhou, R. Yang, G. Chen and M. S. Dresselhaus, *Phys Rev Lett*, 2011, **107**, 226601.
- 13 C. Jeong, R. Kim and M. Lundstrom, *J Appl Phys*, 2011, **111**, 113707.
- 14 G. D. Mahan, *Solid State Physics (N. Y., 1955)*, 1997, **51**, 81–157.
- 15 D. M. Rowe, V. L. Kuznetsov, L. A. Kuznetsova and G. Min, *J Phys D Appl Phys*, 2002, **35**, 315.
- 16 E. Laube, *Monatsh Chem*, 1966, **97**, 722–732.
- 17 Z. Zhu and A. D. Pelton, *J Alloys Compd*, 2015, **641**, 261–271.
- 18 F. Akbar, I. Čurlík, M. Reiffers and M. Giovannini, *J Alloys Compd*, 2024, **976**, 173195.
- 19 I. Sakamoto, S. Ohara, I. Oguro, E. Yamamoto, Y. Haga, Y. Onuki and S. Maruno, *J Alloys Compd*, 1998, **275–277**, 505–509.
- 20 B. Bradlyn, L. Elcoro, J. Cano, M. G. Vergniory, Z. Wang, C. Felser, M. I. Aroyo and B. A. Bernevig, *Nature*, 2017, **547**, 298–305.
- 21 M. G. Vergniory, L. Elcoro, C. Felser, N. Regnault, B. A. Bernevig and Z. Wang, *Nature*, 2019, **566**, 480–485.
- 22 M. G. Vergniory, B. J. Wieder, L. Elcoro, S. S. P. Parkin, C. Felser, B. A. Bernevig and N. Regnault, *Science (1979)*, , DOI:10.1126/science.abg9094.
- 23 P. Giannozzi, S. Baroni, N. Bonini, M. Calandra, R. Car, C. Cavazzoni, D. Ceresoli, G. L. Chiarotti, M. Cococcioni, I. Dabo, A. Dal Corso, S. de Gironcoli, S. Fabris, G. Fratesi, R. Gebauer, U. Gerstmann, C. Gougoussis, A. Kokalj, M. Lazzeri, L. Martin-Samos, N. Marzari, F. Mauri, R. Mazzarello, S. Paolini, A. Pasquarello, L. Paulatto, C. Sbraccia, S. Scandolo, G. Sclauzero, A. P. Seitsonen, A. Smogunov, P. Umari and R. M. Wentzcovitch, *J Phys Condens Matter*, 2009, **21**, 395502.
- 24 J. P. Perdew, K. Burke and M. Ernzerhof, *Phys Rev Lett*, 1996, **77**, 3865–3868.
- 25 M. Topsakal and R. M. Wentzcovitch, *Comput Mater Sci*, 2014, **95**, 263–270.
- 26 G. K. H. Madsen and D. J. Singh, *Comput Phys Commun*, 2006, **175**, 67–71.
- 27 Topological materials database, <https://www.topologicalquantumchemistry.com/#/>.
- 28 G. D. Mahan and J. O. Sofo, *Proceedings of the National Academy of Sciences*, 1996, **93**, 7436–7439.
- 29 Y. B. Kuzma, P. I. Kripyakevich and D. P. Frankevich, *IZV AKAD NAUK SSSR NEORGAN MATERIALY*, 1965, **1**, 1547–1553.